



Co-nanocasting synthesis of mesoporous Cu–Mn composite oxides and their promoted catalytic activities for gaseous benzene removal

Wenxiang Tang^{a,b}, Xiaofeng Wu^a, Shuangde Li^a, Xin Shan^{a,b}, Gang Liu^{a,b}, Yunfa Chen^{a,*}

^a Institute of Process Engineering, Chinese Academy of Sciences, Beijing 100190, China

^b University of Chinese Academy of Sciences, Beijing 100049, China

ARTICLE INFO

Article history:

Received 25 March 2014

Received in revised form 16 May 2014

Accepted 18 June 2014

Available online 26 June 2014

Keywords:

Cu–Mn composite oxide

Nanocasting

Mesoporous structure

Catalytic oxidation

Benzene

ABSTRACT

Mesoporous Cu–Mn oxides with high surface area ($\sim 221 \text{ m}^2 \text{ g}^{-1}$) were successfully obtained through a simple co-nanocasting approach using siliceous SBA-15 mesoporous material as a hard template. Their catalytic performances for deep oxidation of benzene were tested and physicochemical properties were characterized in detail by means of N_2 -physisorption, XRD, XPS, H_2 -TPR, SEM-EDX and TEM. The as-prepared mesoporous Cu–Mn oxides display superior catalytic activity and the temperature required for achieving a benzene conversion of 90% has been obtained at about 234°C over sample $\text{Cu}_{0.6}\text{Mn}$, which is 131°C lower than that on the Cu–Mn oxide prepared by co-precipitation method using NaOH. The apparent activation energy over nanocasted catalyst was low to 45.0 kJ mol^{-1} . Nanocasting process provides a limited nanoreactor for the formation of Cu–Mn composite oxide which makes the Cu–Mn oxides owing small particle size, high surface area, rich surface adsorbed oxygen species, low temperature reducibility and promoting interaction of Cu–Mn species. These characters generated by nanocasting method are responsible for its better catalytic activity.

© 2014 Elsevier B.V. All rights reserved.

1. Introduction

Volatile organic compounds (VOCs) emitted from industrial process, fossil fuels' combustion and biogenic system are dangerous air pollutants and related to many environmental problems, such as photochemical smog and ozone generation [1,2]. Low concentration of VOCs will be a great threat to the health of human beings [3] and the abatement of VOCs is highly desirable. Compared with the traditional methods such as absorption, thermal combustion and biofiltration [4–6] used to remove hazardous VOCs, catalytic oxidation [7,8] is markedly energy-saving to reduce VOCs at low concentration by providing carbon dioxide and water as final products and can keep a good performance longer at lower temperature ($300\text{--}600^\circ\text{C}$) with a great economic advantage. Supported noble metal as Pt, Pd, Au, Ag catalysts [9–11] are known to be active for deep oxidation of VOCs at low temperature which have been used in industrial process widely in abatement of exhausts. However, some drawbacks such as their high cost and other related problems (volatility, sintering, and susceptibly poisoning tendency) prevent a more general application. Metal oxides (Fe_2O_3 , Cr_2O_3 , CuO, NiO, CeO_2 , MnO_2 and Co_3O_4) [12–14] can be obtained easily and are

proved to be active for deep oxidation of VOCs, which are expected to be a better alternative to replace the precious metal catalysts. The synergistic effects are found to be present in different composite oxides such as Mn–Ce–O [15,16,17,18], Co–Ce–O [19,20], Mn–Co–O [18,21,22], Ce–Sn–O [23,24], Cu–Ce–O [25] and Cu–Mn–O [22,26] and it can promote their catalytic activities significantly. However, there are still challenges and opportunities in developing the synergistic effects for mixed metal oxides catalysts with high catalytic activity to the maximum degree. Recently, the synergistic effect has been created and developed via various methods such as the fabrication of core–shell structures [27,28], porous structures [29], ultrafine nanoparticles [30], nanoalloys [29,31], doping oxides [25,32], solid solution [15,23,33] etc. Both creating a highly active interface between different species and making different metal ions exist in the same crystal structure can promote the activities of catalysts significantly. In the past several years, numerous nonsilica mesoporous materials, such as mesoporous carbon [34,35], metal oxides [36–41] and sulfide [42] have been successfully prepared by nanocasting method. The nanocasting technique can induce the fabrication of products taking place in the nanospaces just like nanoreactors provided by the pores of a porous template and the template framework is selectively removed after the synthesis of the material. Therefore, it provides a simple method to strengthen the synergistic effect on account of the fact that the process takes place in a limited nanospace, and the sintering of the particles is

* Corresponding author. Tel.: +86 10 8254 4896; fax: +86 10 8254 4896.

E-mail addresses: yfchen@mail.ipe.ac.cn, chenyf@ipe.ac.cn (Y. Chen).

restricted in the limited nanopores and the achieved materials have high surface area and special nanostructure.

The present study was aimed at promoting the synergistic effect of Cu–Mn composite oxide by nanocasting method. The sintering of Cu–Mn composites was limited in the nanospace (nanopores of SBA-15) which led to the formation of particular mesoporous nanostructure. Catalytic deep oxidation of benzene was act as a model reaction for investigating the activities of synthesized Cu–Mn mesoporous nano-composites compared with others prepared by traditional methods. Our approach in this work holds a significant promise for the design and fabrication of mesoporous metal oxides with enhanced synergistic effects and superior VOCs abatement reactivity.

2. Experimental

2.1. Catalyst preparation

2.1.1. Nanocasting for synthesis of mesoporous Cu–Mn–O nanocomposites

SBA-15 silica was prepared by the classical method and this hard template was calcined in air at 550 °C for 5 h with a heating rate of 2 °C min^{−1}. A simple “two-solvent” approach was firstly used to obtain mesoporous Cu–Mn mixed oxides. In a typical synthesis of catalysts, a certain amount of Cu(NO₃)₂·3H₂O (99.9%, Xilong) solid (0, 0.5, 1.0, 2.0, 3.0, 4.0 g) was dissolved in 5.0 g 50% Mn(NO₃)₂ (50 wt%, Xilong) solution to form a high concentration Cu–Mn mixed solution. 2.5 g mesoporous SBA-15 was dispersed in 120 ml of dry *n*-hexane. After stirring at room temperature for 4 h, a desired volume of Cu–Mn mixed solution (quantity corresponding to the pore volume of SBA-15 template determined by N₂ sorption) was added slowly with stirring. The mixture was stirred vigorously for 12 h at room temperature. Afterwards, the samples were filtered and dried at 40 °C for 48 h. All samples were calcined at 450 °C for 5 h (with the heating rate of 2 °C min^{−1}) in ambient air. The resulting materials were treated three times with a 2 M NaOH solution in water, to remove the silica template, and washed with water and ethanol several times, then dried at 80 °C. The mesoporous Cu–Mn mixed oxides which were denoted as Cu₀Mn, Cu_{0.15}Mn, Cu_{0.3}Mn, Cu_{0.6}Mn, Cu_{0.9}Mn, and Cu_{1.2}Mn were formed in this procedure.

2.1.2. Cu–Mn composite oxides synthesized by other methods

2.1.2.1. Coprecipitation. Typically, 2.0 g Cu(NO₃)₂·3H₂O and 5.0 g 50 wt% Mn(NO₃)₂ solution (the catalytic activity of the mesoporous sample synthesized in this ratio was the best in this research) were added to 100 ml deionized water (18.0 MΩ cm) to form a mixed solution. Then the NaOH (or Na₂CO₃) solution (2.2 g NaOH or 2.8 g Na₂CO₃ were dissolved in 100 ml deionized water) was slowly added to the above mixed solution accompanied by vigorously stirring and aged for 4 h at room temperature. The resulting precipitate was filtered and washed three times with water and ethanol, dried at 80 °C for 12 h. The samples were heated at 450 °C for 5 h (heating rate 2 °C min^{−1}) in air and denoted as B-Cu_{0.6}Mn–NaOH (NaOH route) and C-Cu_{0.6}Mn–Na₂CO₃ (Na₂CO₃ route).

2.1.2.2. Direct calcination. 2.0 g Cu(NO₃)₂·3H₂O was dissolved in 5.0 g 50 wt% Mn(NO₃)₂ solution to form a high concentration of Cu–Mn mixed solution. This solution was calcined directly at 450 °C for 5 h (heating rate 2 °C min^{−1}) in air and the obtained material was denoted as D-Cu_{0.6}Mn–DC.

2.2. Catalyst characterization

The BET specific surface area and pore size distributions of all catalysts were obtained with N₂ adsorption–desorption method on an automatic surface analyzer (AS-1-C TCD, Quantachrome Corp.,

USA). Before measurement, every sample was degassed at 200 °C for 3 h. Powder X-ray diffraction (XRD) patterns of the catalysts were measured on a Panalytical X'Pert PRO system using Cu–Kα radiation in the diffraction angle (2θ) range 5–90°. Crystal phase were identified by using the X'pert HighScore software to refer the related peaks to the standard powder diffraction in database (ICDD PDF2-2004). The composition, texture, and distribution of the catalysts were also characterized by field-emission scanning electron microscopy (SEM) via an electron microscope (JEOL 2100F, operating at 15 kV), equipped with an energy dispersive X-ray detector. The microstructures of samples were recorded using transmission electron microscopy (TEM) (JEOL JEM-2010F) with an accelerating voltage of 200 kV. Surface species of the as-prepared catalysts were determined by X-ray photoelectron spectroscopy (XPS) using an XLESCALAB 250Xi electron spectrometer from VG Scientific with a monochromatic Al Kα radiation. Hydrogen temperature programmed reduction (H₂-TPR) was carried out in a U-shaped quartz reactor under a gas flow (5% H₂ balanced with Ar, 25 ml min^{−1}) with Automated Catalyst Characterization System (Autochem 2920, MICROMERITICS). In each procedure, about 30 mg catalyst (40–60 mesh) was used and the temperature was raised to 700 °C from room temperature at a constant rate of 10 °C min^{−1}.

2.3. Catalytic activity testing

Catalytic activity evaluation was carried out in a continuous flow quartz fixed-bed reactor (i.d. 6 mm) and 100 mg catalyst (40–60 mesh) diluted with 0.3 g of quartz sands was placed in the middle of the tube-reactor with the aid of glass wool. The total gas flow rate (100 ml min^{−1}) was adjusted to a space velocity of (SV) = 60,000 ml g^{−1} h^{−1} and the concentration of benzene used was about 1000 ppm (air balanced). The catalyst was pre-treated in the reactant flow at 100 °C for 1 h before each testing. The effluent gas was separated by a capillary column (Stabilwax-DA, 0.53 mm × 0.5 μm × 30 m) and the concentration of benzene was analyzed by a gas chromatograph (GC-2014, Shimadzu) equipped with a flame ionization detector (FID). The concentration of CO₂ in the outlet gas was detected by another FID with a methanizer (MTN, Shimadzu) to convert CO₂ to CH₄ (the conversion > 99.5%). The complete conversion value of benzene (η_{benzene} %) was calculated according to the following equation:

$$\eta_{\text{benzene}}\% = \frac{(\text{CO}_2)_{\text{out}}}{((\text{C}_6\text{H}_6)_{\text{in}} \times 6)} \times 100$$

where (CO₂)_{out} (ppm) and (C₆H₆)_{in} (ppm) were the concentrations of CO₂ in the outlet gas and benzene in the inlet gas, respectively.

For consideration of the water vapor's effect on the catalytic activity of the Cu_{0.6}Mn catalyst obtained by different methods, the on-stream benzene oxidation experiments were carried out in the presence and absence of 1.5 vol% water vapor. Typically, an air flow (50 ml min^{−1}) was used for bubbling water before mixed with another air flow containing gaseous benzene and the mixed gas that composed a relative water vapor (1.5 vol%) and benzene (500 ppm) was used for catalytic test.

2.4. Reaction kinetics testing

The kinetics parameters were measured in the fixed-bed reactor for benzene oxidation, as mentioned above, and the catalytic reaction data were obtained after the reaction was stable for 60 min with a C₆H₆ complete conversion lower than 20% at different temperatures. The reaction rate (*r*, mol g_{cat}^{−1} s^{−1}) of benzene conversion was calculated as the following equation,

$$r_{\text{C}_6\text{H}_6} = \frac{N_{\text{C}_6\text{H}_6} \times \eta_{\text{C}_6\text{H}_6}}{W_{\text{cat}}} \quad (1)$$

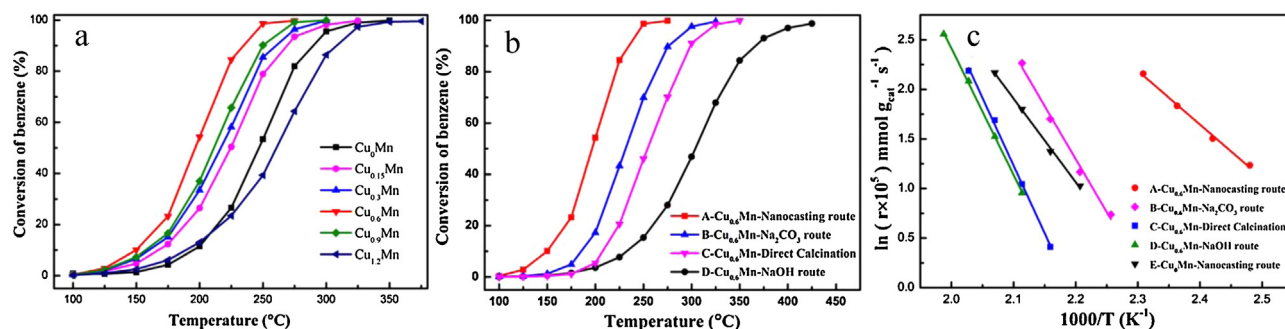


Fig. 1. ((a) and (b)) Benzene conversion as a function of reaction temperature over Cu–Mn composite oxides prepared by nanocasting strategy and other methods, (c) Arrhenius plots for the oxidation of benzene over the Cu–Mn composite oxides synthesized by different methods.

where $N_{C_6H_6}$ was the C_6H_6 gas flow rate (mols⁻¹), W_{cat} was the catalyst weight (g). A good linear Arrhenius plots for the oxidation of VOC could be obtained by assuming a first-order kinetics with respect to VOC and a zero-order kinetics with respect to oxygen on oxide catalysts in many publications [43–45]. When the conversion of benzene was below 20%, the dependence of the reaction rate ($r_{C_6H_6}$) on the products of CO_2 and H_2O might be ignored. Therefore, it could be reasonably assumed that in the case of excessive oxygen, benzene oxidation would obey a first-order reaction mechanism with respect to benzene concentration (c , mol g⁻¹):

$$r_{C_6H_6} = \left(-A \exp \left(\frac{-E_a}{RT} \right) \right) c \quad (2)$$

where A was the pre-exponential factor and E_a was the apparent activation energy (kJ mol⁻¹). The activation energy (E_a) could be obtained from the slope of the resulting linear plot of $\ln r$ versus $1/T$.

3. Results and discussion

3.1. Catalytic performances and kinetic parameters

Fig. 1a shows the catalytic activity of the mesoporous Cu–Mn composite oxides prepared by nanocasting approach. It can be seen clearly that all catalysts could completely convert benzene to CO_2 below 325 °C and no other by-product was detected at end of the reaction. Compared with the single mesoporous manganese oxide, the addition of Cu improves the catalytic performance significantly and the sample Cu_{0.6}Mn exhibits much better than others. However, the catalytic activity will decrease obviously when the mole ratio of Cu/Mn is more than 0.6 (Cu_{0.9}Mn, Cu_{1.2}Mn) which confirms that higher content of Cu will inhibit its promoting effect of catalysts. The effect of preparation method on Cu_{0.6}Mn catalyst for catalytic removal of benzene was examined and the results are shown in Fig. 1b. The reaction temperatures of $T_{10\%}$, $T_{50\%}$ and $T_{90\%}$ (corresponding to benzene conversion into CO_2 = 10, 50 and 90%) were used to compare the catalytic activities of the catalysts, as summarized in Table 1. It is found that the Cu_{0.6}Mn-nanocasting sample performed the highest catalytic activity, and the $T_{50\%}$ and $T_{90\%}$ were 196 and 234 °C which were 99 and 131 °C lower

than those achieved over the NaOH-derived sample B-Cu_{0.6}Mn, respectively. Meanwhile, the reaction rate at 250 °C over the Cu_{0.6}Mn-nanocasting sample was 7.32×10^{-4} mol g_{cat}⁻¹ s⁻¹ which was four times higher than that (1.44×10^{-4} mol g_{cat}⁻¹ s⁻¹) of the NaOH-derived sample B-Cu_{0.6}Mn. It is worth pointing out that the catalytic performance over nanocasted Cu–Mn composite oxide was much higher than other reported publication [13,14,17,46,47], further indicating the nanocasting method is an effective way to promote the catalytic performance of materials.

The catalytic performance can also be evaluated by comparing the E_a values of different catalysts and the sample with lower E_a value will perform superior catalytic activity. The Arrhenius plots for the oxidation of benzene at conversion below 20% (at which the reaction temperature was in the range of 120–220 °C) over the Cu–Mn composite oxide catalysts prepared by different methods are displayed in Fig. 1c. The plots of $\ln r$ versus $1/T$ perform excellent linear relationships (the correlation coefficients (R^2) were rather close to 1) and the activation energies (E_a) obtained from the slopes of the linear plots are listed in Table 1. The E_a value (69.8 kJ mol⁻¹) of the single MnO_x catalyst was much higher than that (45.0 kJ mol⁻¹) of nanocasted sample A-Cu_{0.6}Mn which confirms the promoting effect of Cu. It is also observed that the nanocasted Cu_{0.6}Mn catalyst possessed the lowest E_a values (45.0 kJ mol⁻¹) among the Cu_{0.6}Mn catalysts prepared by different methods which confirms the advantage of nanocasting strategy.

In order to examine the stabilities and effect of water vapor on the catalytic performances of the as-prepared Cu_{0.6}Mn catalysts, the on-stream benzene conversion into CO_2 experiments at a certain temperature (260 °C) were carried out in the absence and presence of 1.5 vol% water vapor as shown in Fig. 2. The results present that there was no significant drop in catalytic oxidation of benzene within the first 12 h of on-stream reaction over all catalysts. It is found that only ca. 4% loss in benzene conversion over nanocasted Cu_{0.6}Mn catalyst when 1.5 vol% water vapor was introduced to the gas feed while the values were ca. 14, 22 and 7 over the B, C and D sample, respectively. When water vapor was cut off, the conversion of benzene restored to the original values and kept stable in the next 12 h, indicating the effect of water vapor in this reaction system is negative which may be due to the competitive adsorption of water and organic molecules. However, the conversion after 36 h

Table 1
Benzene oxidation, reaction rates at 250 °C, apparent activation energy and correlation coefficients (R^2) of the plot $\ln k$ versus inverse temperature for the oxidation of benzene over the Cu–Mn catalysts prepared by different methods.

| Sample | $T_{10\%}$ (°C) | $T_{50\%}$ (°C) | $T_{90\%}$ (°C) | Reaction rate at 250 °C ($\times 10^{-4}$ mmol g _{cat} ⁻¹ s ⁻¹) | E_a (kJ mol ⁻¹) | R^2 |
|------------------------|-----------------|-----------------|-----------------|--------------------------------------------------------------------------------------------------|-------------------------------|-------|
| Cu _{0.6} Mn | 196 | 247 | 290 | 3.97 | 69.8 | 0.997 |
| A-Cu _{0.6} Mn | 150 | 196 | 234 | 7.32 | 45.0 | 0.994 |
| B-Cu _{0.6} Mn | 233 | 305 | 365 | 1.44 | 106.4 | 0.999 |
| C-Cu _{0.6} Mn | 183 | 231 | 277 | 5.21 | 89.1 | 0.991 |
| D-Cu _{0.6} Mn | 208 | 255 | 300 | 3.43 | 113.1 | 0.998 |

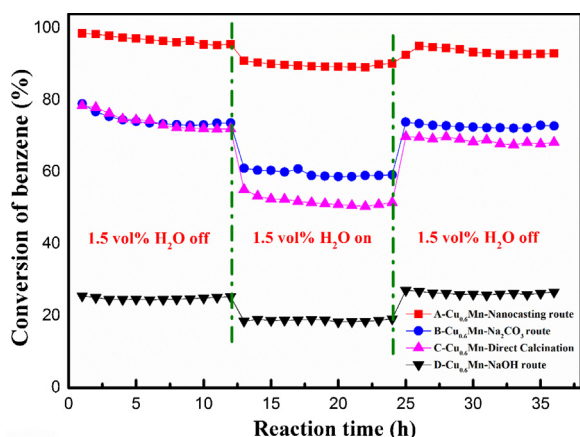


Fig. 2. Effect of water vapor on the catalytic activities of $\text{Cu}_{0.6}\text{Mn}$ composite oxides prepared by different method for benzene oxidation at 260°C . Benzene concentration = 500 ppm, water concentration = 1.5 vol% and $\text{SV} = 60,000 \text{ ml g}^{-1} \text{ h}^{-1}$.

testing over the nanocasted catalyst is above 93.0% which performs much better than the other samples prepared by different methods.

3.2. Crystal phase, surface area and pore distribution

The XRD patterns of the as-prepared composite oxides are shown in Fig. 3. The main diffractions of single manganese oxide without Cu (Cu_0Mn) can be indexed to MnO_2 (JCPDS PDF 001-0799). It can be observed that a clear peak at $2\theta = 12.3^\circ$ was ascribed to the (001) crystal planes of birnessite MnO_2 (JCPDS 043-1456) for sample $\text{Cu}_{0.15}\text{Mn}$ and this transformation may be attributed to the addition of a small content of Cu species which can keep stable in the interlayer or tunnel structure of birnessite MnO_2 [48,49]. With increasing the content of Cu, all the XRD patterns (Fig. 3) show a few broad diffraction peaks that are difficult to assign, especially to a particular composition $\text{Cu}_{1.5}\text{Mn}_{1.5}\text{O}_4$ (JCPDS 35-1172) or CuMn_2O_4 (JCPDS 34-1322). The low angle XRD diffraction patterns of the nanocasted samples are displayed in Fig. S2. Low-angle XRD of siliceous template shows a well-resolved pattern with a

prominent peak at 0.9° , and two peak at 1.6° and 1.8° 2θ , which is agreement with the pattern reported for SBA-15 [50]. However, the reflections of nanocasted samples are broad and low in intensity, suggesting that these hopcalite composites are less ordered than their silica template. The low intensity of low-angle XRD observed on the nanocasted samples may be attributed to the symmetry destroying by the removal of template and insufficiency of the remained guest matter (Cu–Mn oxides), which has often been obtained for replicas from silica templates [36,51–54]. Compared with other Cu–Mn oxides synthesized by different approaches, it is easy to form solid solution on the NaOH- and Na_2CO_3 -derived products except the mixed oxides prepared by direct calcination method. It can be found that the peaks of Cu–Mn solid solution are weak on sample C and most of diffraction peaks shown can be corresponded to monoclinic crystal CuO (JCPDS 001-1117). This result indicates that the limited nanocasting strategy is better for formation of solid solution oxides because of its limited nanospace provided by hard template. According to the Scherrer equation, the grain size of as-prepared catalysts can be calculated by using the full width at half maximum of strongest peak and the results are listed in Table 2. Apparently, the grain size of nanocasted $\text{Cu}_{0.6}\text{Mn}$ was 10.8 nm which was the smallest particle among the prepared samples and more active sites will be introduced over the smallest nanoparticles. Hence, the catalytic activity over nanocasted $\text{Cu}_{0.6}\text{Mn}$ catalyst will be better.

Fig. 4 displays the N_2 adsorption–desorption isotherms and the pore size distribution of the as-prepared catalysts. The isotherms of the nanocasted materials show type IV characteristics with well-developed H1 type hysteresis loops which are related to the capillary condensation in mesopores, indicating the mesoporous structure of catalysts [55]. Moreover, a typical H3 type hysteresis loop is shown on the Cu–Mn oxides obtained by other methods which is ascribed the existence of mesopores or macropores formed by aggregation of nanoparticles. The textural parameters of all samples are summarized in Table 2. The surface area and pore volume of nanocasted catalysts were, respectively, up to $266 \text{ m}^2 \text{ g}^{-1}$ and $0.858 \text{ cm}^3 \text{ g}^{-1}$ and obviously higher than that of the others prepared by different approaches which are due to the removal of hard silicon template. Many reports have demonstrated that high surface

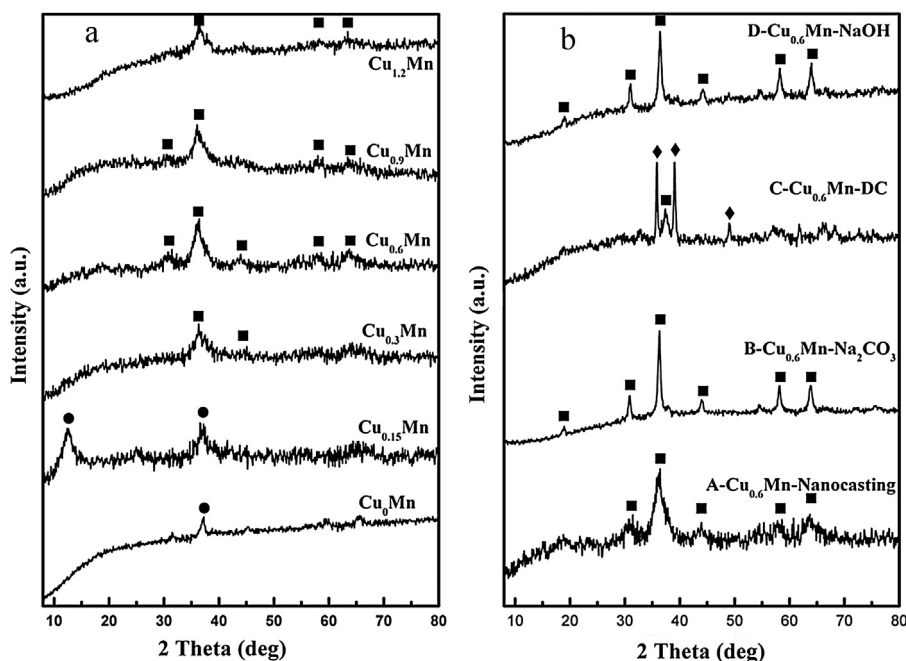


Fig. 3. XRD patterns of the Cu–Mn composite oxides prepared by nanocasting strategy (a) and other methods (b) (● MnO_2 , ■ $\text{Cu}_{1.5}\text{Mn}_{1.5}\text{O}_4$ or CuMn_2O_4 , ♦ CuO).

Table 2
Surface areas, average pore sizes, and pore volumes from BET analysis and surface element compositions of the Cu–Mn samples from the Mn 2p, Cu 2p and O 1s XPS spectra.

| Sample | BET surface area (m ² g ^{−1}) | Pore size (nm) | Pore volume (cm ³ g ^{−1}) | <i>D</i> ^a (nm) | Surface element molar ratio | | | | | | | |
|------------------------|----------------------------------------------------|----------------|------------------------------------------------|----------------------------|-----------------------------|------------------|------------------------------------|-----------------|------------------|-------------------|------------------|-------------------------------------|
| | | | | | Mn ³⁺ | Mn ⁴⁺ | Mn ⁴⁺ /Mn ³⁺ | Cu ⁺ | Cu ²⁺ | O _{latt} | O _{ads} | O _{ads} /O _{latt} |
| Cu ₀ Mn | 132.6 | 17.5 | 0.587 | 13.4 | – | – | – | – | – | – | – | – |
| Cu _{0.15} Mn | 149.5 | 3.8 | 0.221 | 12.7 | – | – | – | – | – | – | – | – |
| Cu _{0.3} Mn | 221.2 | 13.8 | 0.572 | 26.8 | – | – | – | – | – | – | – | – |
| A-Cu _{0.6} Mn | | | | | | | | | | | | |
| Cu _{0.9} Mn | 266 | 9.5 | 0.858 | 14.1 | – | – | – | – | – | – | – | – |
| Cu _{1.2} Mn | 121 | 3.7 | 0.308 | 14.8 | – | – | – | – | – | – | – | – |
| B-Cu _{0.6} Mn | | | | | | | | | | | | |
| C-Cu _{0.6} Mn | | | | | | | | | | | | |
| D-Cu _{0.6} Mn | | | | | | | | | | | | |

^a Data calculated based on the XRD results according to the Scherrer equation using the FWHM of the strongest peak line of samples.

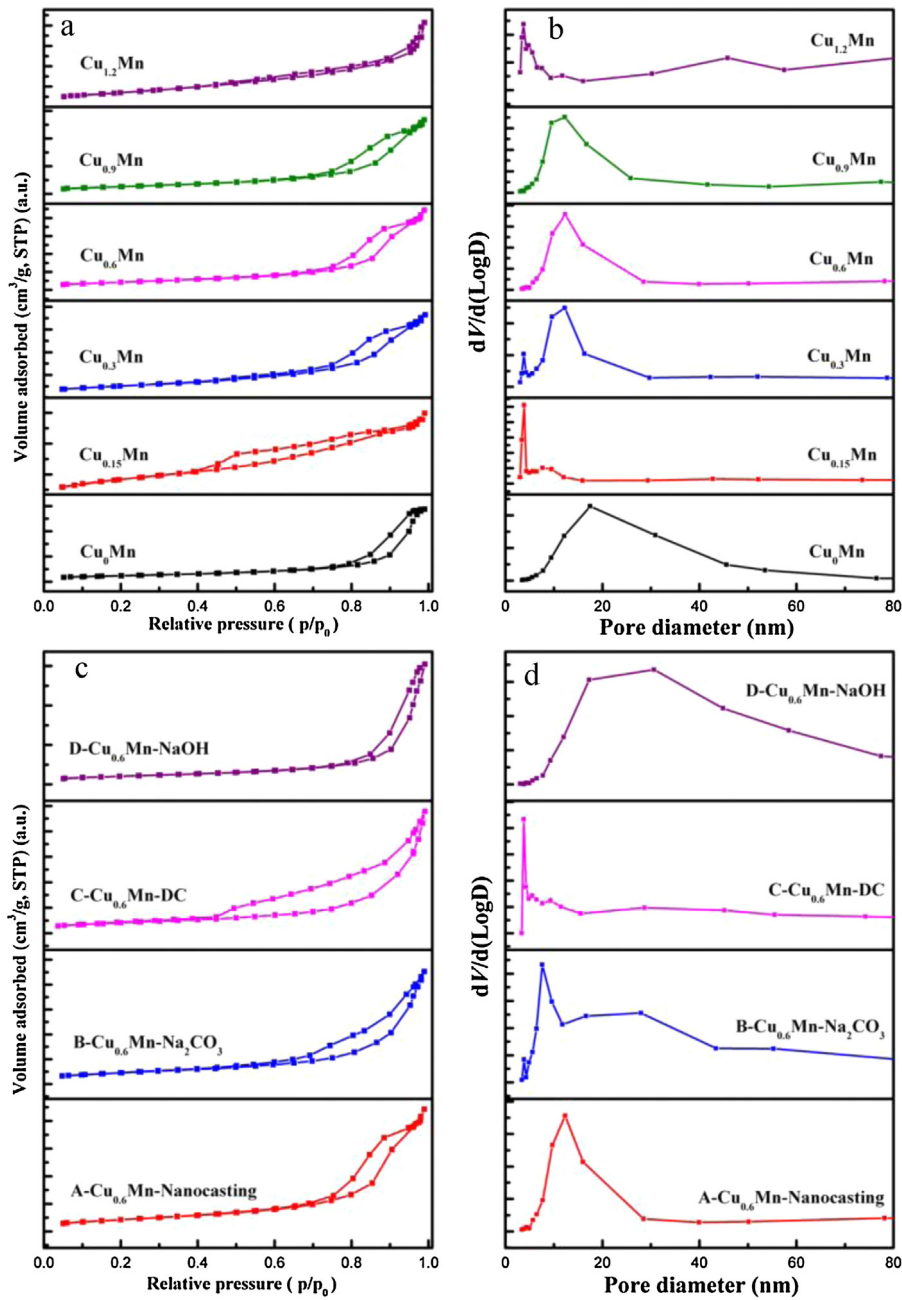


Fig. 4. N₂ adsorption–desorption isotherms and pore-size distribution of the Cu–Mn composite oxides prepared by nanocasting strategy ((a) and (b)) and other methods ((c) and (d)).

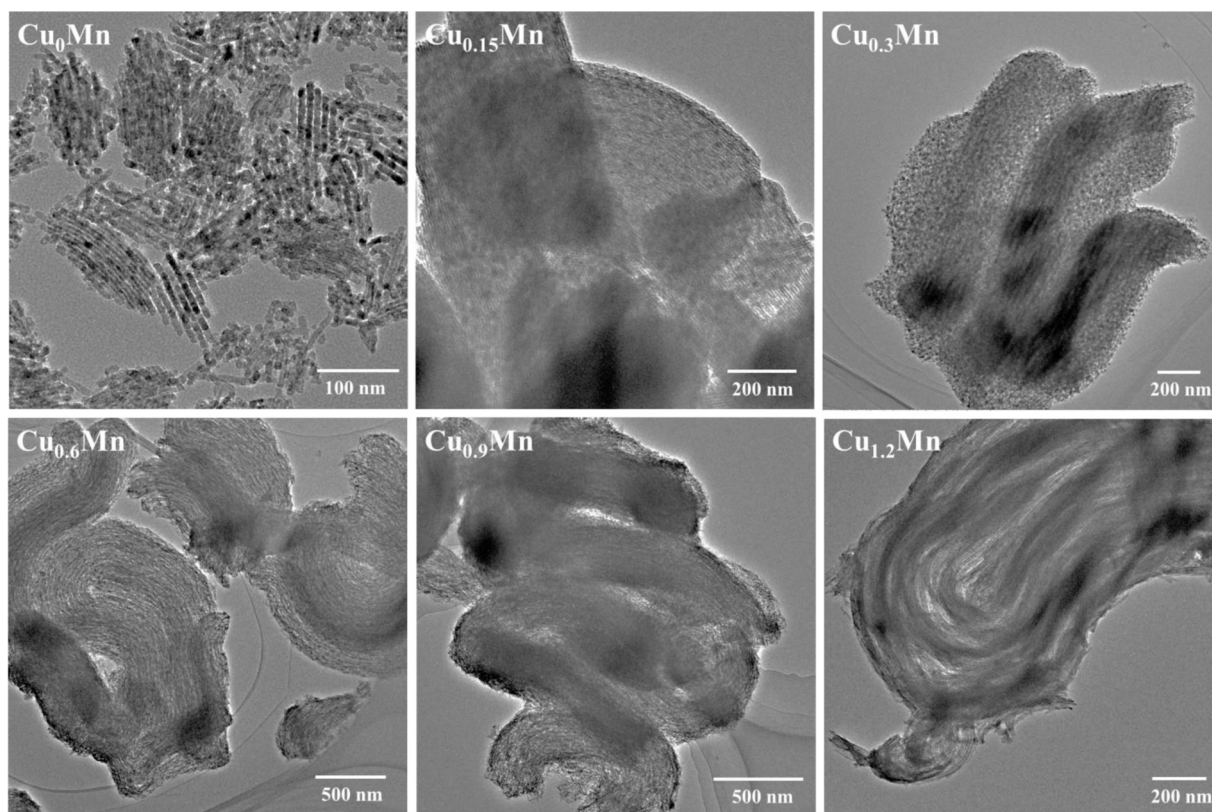


Fig. 5. TEM images of the Cu–Mn composite oxides prepared by nanocasting strategy.

area could provide more active sites and rich pore structure would be better for the adsorption and diffusion of reactant molecules [9,11,25,56,57]. Therefore, the high surface area and pore volume developed by nanocasting method can make a great contribution on the catalytic activity for benzene oxidation even though the highly ordered structure from SBA-15 was not kept very well.

In addition, the BET analyses of used samples were carried and the results are shown in Table S1. As displayed in Table S1, the surface area of nanocasted sample has a clear reduction while the other samples prepared by different methods have no obvious variation. For the nanocasted sample, the surface area decreased to $161.0 \text{ m}^2 \text{ g}^{-1}$ from $211.7 \text{ m}^2 \text{ g}^{-1}$ and the pore volume reduced to $0.58 \text{ cm}^3 \text{ g}^{-1}$ from $0.7 \text{ cm}^3 \text{ g}^{-1}$, respectively. According to the process of nanocasting, the template (SBA-15) of calcined sample was removed by NaOH solution directly and no other heat treatment was added until the testing of catalyst under a relative high temperature (260°C). Because of the limited effect of nanocasting method, the nanoparticles of hopcalite were formed in the template's pores and the defective surface (interface between metal oxide nanoparticles and silica) will be exposed after removal of template. This defective surface will be unstable and a slight growth of nanoparticles will take place under the developing temperature with time on line (testing temperature was 260°C), which caused the reduction of surface area and pore volume on the nanocasted sample. Meanwhile, this defective surface would have a better activity for benzene oxidation and the growth of nanoparticles (or reduction of defective surface) would be main reason for the slight of deactivation with time on line. The reaction rates per square meter (specific activity) were calculated by using the surface area and benzene conversion at different temperature and the result was presented in Fig. S3. It can be clearly seen that this reaction rate augmented with the rise in reaction temperature and the order of these catalysts at different temperature zone is inconsistent. For example, when this

value was calculated at lower reaction temperature such as 200°C , the reaction rate over nanocasted sample turned into the highest one while the value obtained at 260°C was the lowest. It seems like that the catalyst with lower surface area has higher specific activity which is similar to the other reports [18,58]. However, it is worth pointing out that the nanocasted sample exhibited higher activity at lower temperature ($<225^\circ\text{C}$) than the other catalysts.

3.3. Morphology, microstructure and element distribution

As shown in Fig. S1, the rope-like hard template (SBA-15) with highly ordered mesoporous structure was synthesized by using P123 as a soft template under acid condition. Nanocasting was carried out by impregnating the template with a highly concentrated solution and the formation of mixed oxides took place in the limited nanospaces under heat treatment, then dissolving the SBA-15 template to leave a replica mesoporous structure. Fig. 5 shows the TEM images of Cu–Mn composite oxides prepared by nanocasting route. It is clearly seen that the rod morphology of template was kept very well except the single manganese oxides. The addition of Cu increased the concentration of impregnated solution which is good for filling the pore spaces and keeping the original structure of template. Moreover, TEM data indicates the mesoporous structure of composite oxides was introduced successfully after removal of template.

The morphologies and microstructures of catalysts prepared by different methods are shown in Figs. 6 and 7. The rod morphology of hard template was kept very well on sample A (nanocasted Cu–Mn composite oxide) which showed a clear mesoporous structure from their TEM observations. From the high-resolution TEM (HRTEM) images of catalyst A, the typical intraplanar spacing was measured to be 0.29 and 0.49 nm which were close to that of the (2 2 0) and (1 1 1) crystal phase of the standard $\text{Cu}_{1.5}\text{Mn}_{1.5}\text{O}_4$ (JCPDS

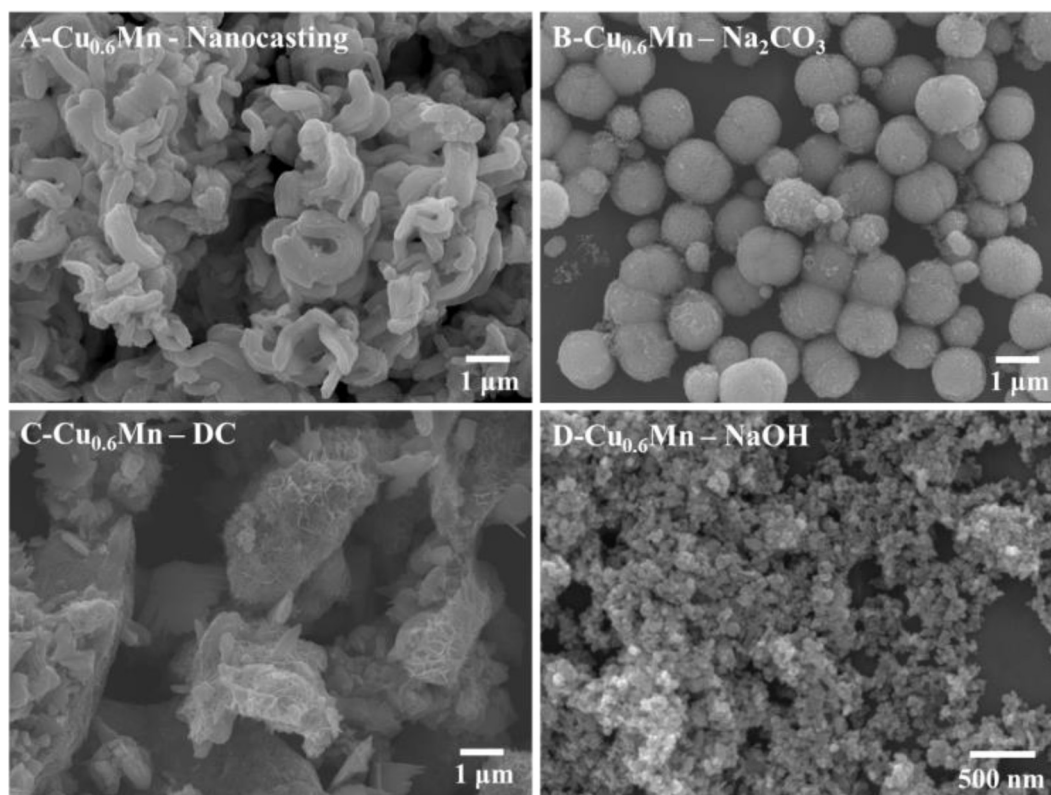


Fig. 6. SEM images of the Cu–Mn composite oxides prepared by different methods.

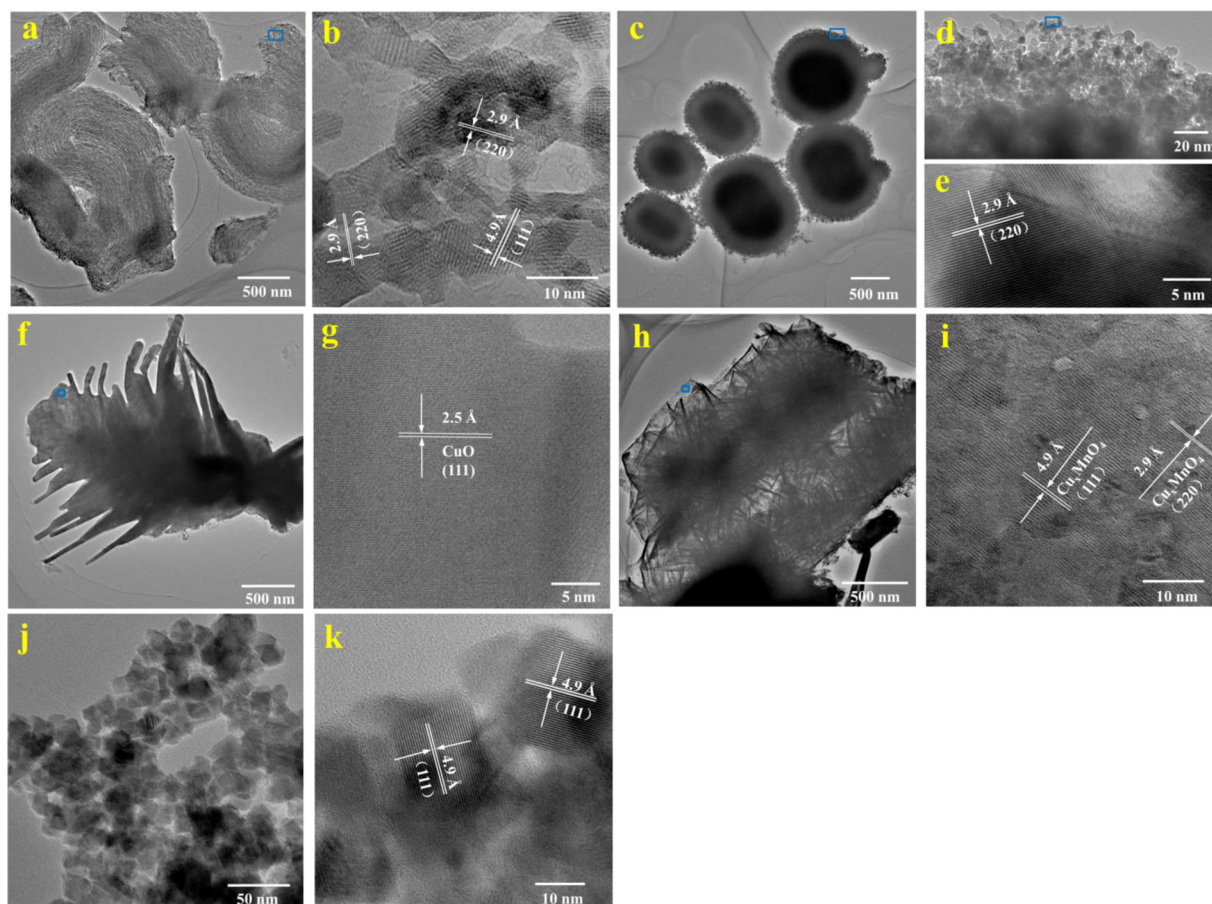


Fig. 7. TEM images of the $\text{Cu}_{0.6}\text{Mn}$ composite oxides prepared by ((a) and (b)) nanocasting strategy ((c), (d) and (e)) Na_2CO_3 route ((f), (g), (h) and (i)) direct calcination ((j) and (k)) NaOH route.

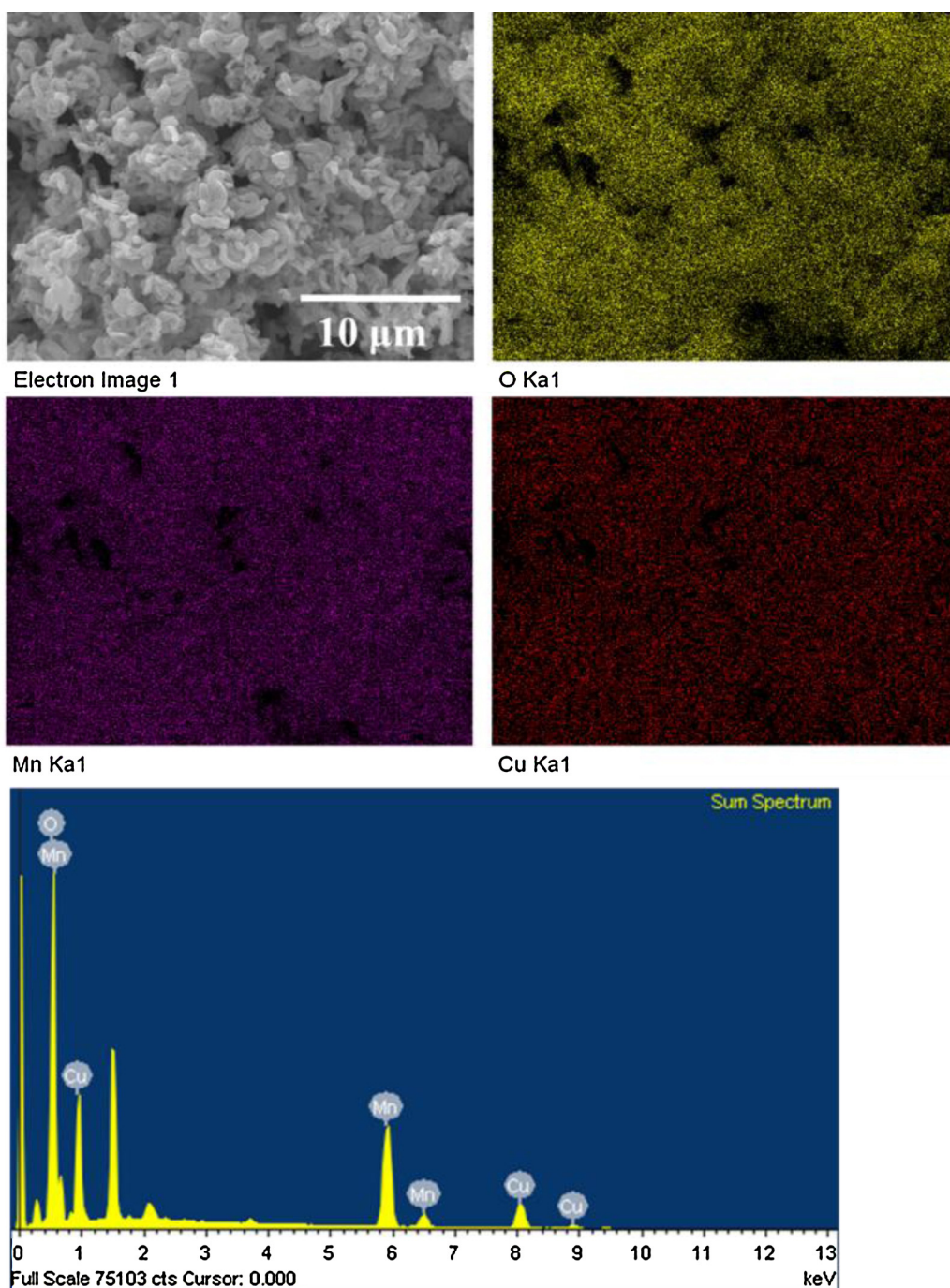


Fig. 8. SEM image, element distribution and EDX data of mesoporous $\text{Cu}_{0.6}\text{Mn}$ composite oxide prepared by nanocasting strategy.

35–1172). A panoramic view of the Na_2CO_3 -derived Cu–Mn oxide reveals that the sample is hamburger-like particles with $\sim 1.0\ \mu\text{m}$ in diameter and $\sim 2.0\ \mu\text{m}$ in length, as shown in Fig. 6. The geometrical structure of as-prepared sample B is further elucidated by TEM method and it is clearly seen that the hamburger-like nanostructure is composed of a large amount of nanoparticles and the disordered wormhole-like pores is clearly observed in the midst of particles. As shown in Fig. 7e, the lattice spacing at 0.29 nm matches well with the (2 2 0) crystal phase of the $\text{Cu}_{1.5}\text{Mn}_{1.5}\text{O}_4$. Direct calcination for preparing sample C under open condition leads to the formation of different structure such as leaf-like and layer-like morphology, as displayed in Fig. 6. The HRTEM images of sample C reveal that the lattice spacing of leaf-like structure is 0.25 nm which can be

assigned to (1 1 1) crystal phase of CuO (JCPDS 01–1117) and the lattice spacing of layer-like structure is about 0.49 and 0.29 nm, rather close to that of the (2 2 0) and (1 1 1) crystal phase of the standard $\text{Cu}_{1.5}\text{Mn}_{1.5}\text{O}_4$ (JCPDS 35–1172). This result demonstrates CuO and Cu–Mn composite oxide are formed simultaneously during the calcination which is agreement with XRD data (shown in Section 3.2). Significantly, it turns out to be that the heat treated environment has a great impact on the as-prepared catalyst and the limited nanospaces provided by hard template is better for formation of solid solution which will promote their catalytic activity. The SEM and TEM images of sample D obtained by NaOH route are presented in Figs. 6 and 7. The particle sizes of catalyst D are quite uniform ($\sim 20\ \text{nm}$) but have obvious agglomeration and the main intraplanar

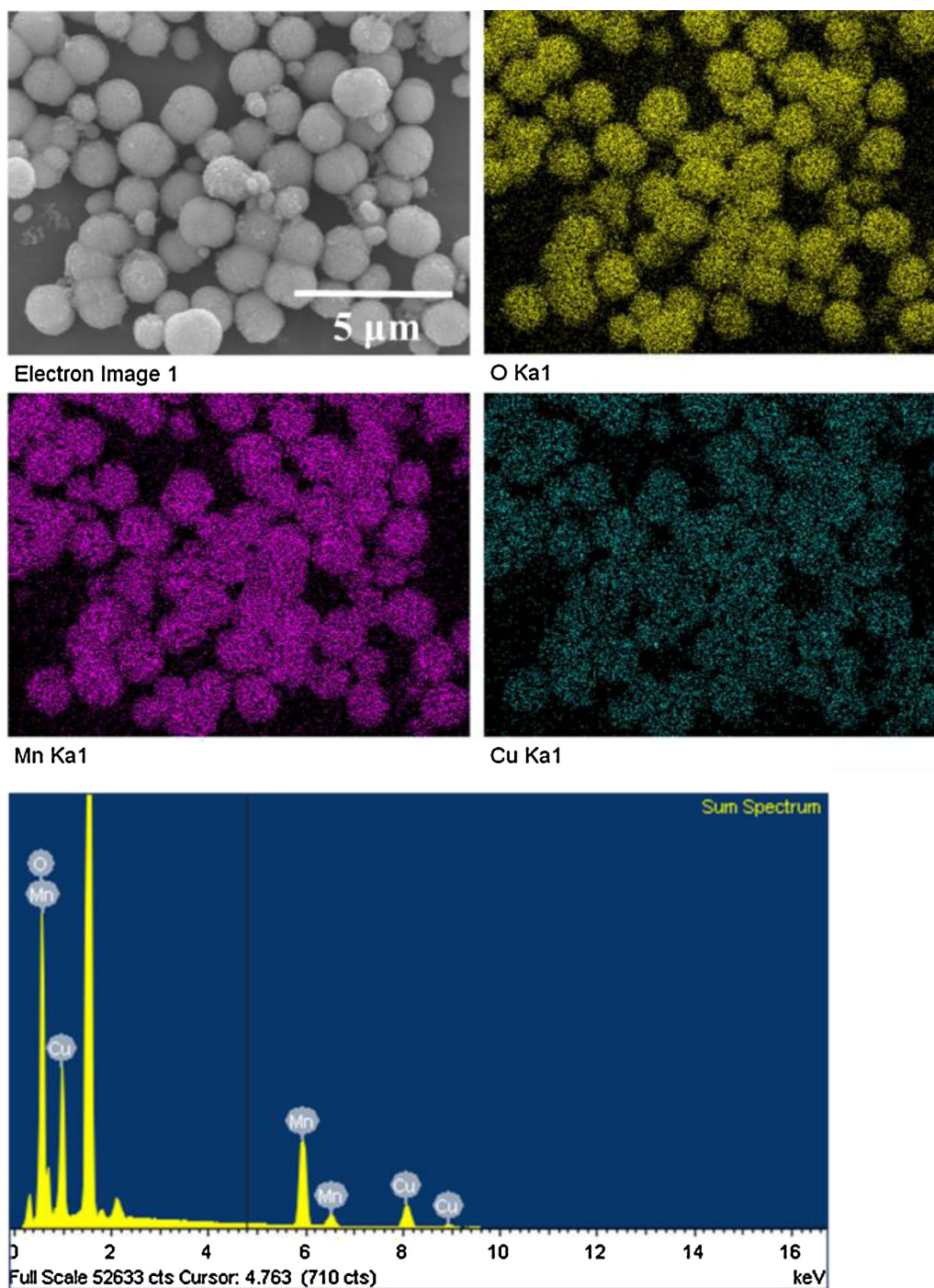


Fig. 9. SEM image, element distribution and EDX data of $\text{Cu}_{0.6}\text{Mn}$ composite oxide prepared by Na_2CO_3 route.

spacing about 0.49 nm can be ascribed to the (1 1 1) crystal plane of the standard $\text{Cu}_{1.5}\text{Mn}_{1.5}\text{O}_4$. Moreover, the microstructure of used nanocasted sample (A) was analyzed by TEM method. As shown in Fig.S4, the porous structure casted from template was kept well after a long time catalytic testing (36 h) even under the humid condition, indicating the good stability of this hopcalite catalyst with high activity which will be a proper candidate for industrial application.

In order to derive information about the element dispersion, the composite oxides prepared by different methods have been tested by SEM–EDX analysis (Figs. 8 and 9, Figs. S5 and S6). As shown in

Fig. 8, EDX mapping of the nanocasted oxide illustrates a uniform distribution of Cu, Mn and O in the particle region and the related peaks can be seen clearly in the spectrum. The other unsigned peaks in the spectrum were Al and Pt which can be ascribed to the aluminized paper substrate (for dispersing sample) and spraying Pt (for creating a conductive layer). Similarly, a desired element distribution is also obtained on the sample B and D (displayed in Fig. 9 and Fig. S6), further indicating the formation of solid solution. However, some separate Cu region without Mn on leaf-like particles can be seen in catalyst C as shown in Fig. S5 (square zone), suggesting direct calcination leads to generation of CuO particles which is

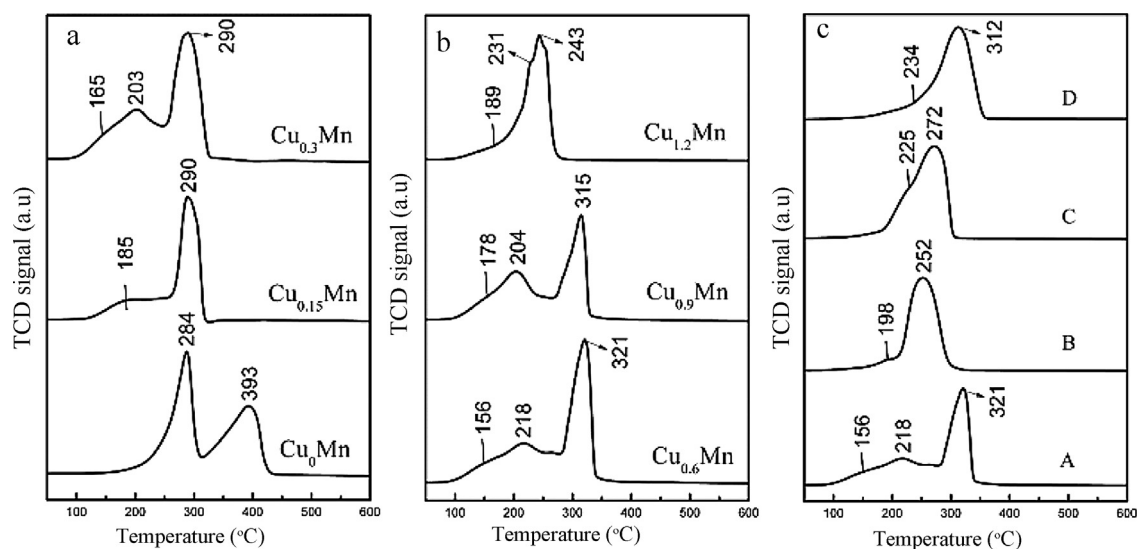


Fig. 10. H_2 -TPR profiles of the Cu–Mn composite oxides prepared by nanocasting strategy ((a) and (b)) and different methods (c).

agreement with the XRD and TEM analysis. Moreover, some typical regions (circle zone in Fig S5) with well dispersion of Cu and Mn confirm the formation of spinel Cu–Mn oxide.

3.4. Temperature-programmed reduction

TPR experiments were performed to investigate the reducibility of as-prepared Cu–Mn oxide as represented in Fig. 10. The single mesoporous manganese oxide without copper exhibits two separate reduction peaks that can be ascribed to the reduction of MnO_x to Mn_3O_4 and Mn_3O_4 to MnO [18,22,26,41,46], shown in Fig. 10a, respectively. With addition of Cu, all of the reduction of peaks of the corresponding samples from $\text{Cu}_{0.15}\text{Mn}$ to $\text{Cu}_{1.2}\text{Mn}$ shifted to lower temperatures, indicating the presence of strong synergistic effect between Mn and Cu species. Because of the higher reducibility of Cu, Mn species are therefore not expected to reduce at lower temperatures so that the low temperature peak are considered to correspond to the reduction of Cu^{2+} [22,26,59]. However, the existence of Cu species (Cu^{2+} or Cu^+) in the mixed oxide will increase the content of Mn^{4+} which can also promote the reduction of MnO_x [26]. Meanwhile, the reduction peaks at lower temperature is assigned to the reduction the chemically adsorbed oxygen species on the Cu–Mn spinel oxide which have a significant effect on the catalytic activities. Apparently, the low-temperature reducibility of samples such as $\text{Cu}_{0.3}\text{Mn}$, $\text{Cu}_{0.6}\text{Mn}$ and $\text{Cu}_{0.9}\text{Mn}$ are the best in the nanocasted catalysts which are good agreement with their excellent performances for catalytic benzene oxidation. Fig. 10c depicts the H_2 -TPR profiles of the Cu–Mn oxides obtained by other methods. All samples exhibit an asymmetrical reduction peak that can be decomposed into two parts, derivable to the reduction of Cu

and Mn species. Significantly, the low-temperature reducibility of nanocasted Cu–Mn catalyst is better than that of the other three samples, suggesting that the strong effect between Cu and Mn can be promoted adequately by co-nanocasting techniques.

3.5. X-ray photoelectron spectroscopy (XPS)

Fig. 11 gives the Mn $2p_{3/2}$, Cu $2p$ and O $1s$ XPS spectra of the Cu–Mn oxides prepared by different methods. As displayed in Fig. 10a, the asymmetrical Mn $2p_{3/2}$ XPS signal of all samples could be decomposed to three components at BE = 641.4, 642.7 and 644.8 eV, ascribable to the surface of Mn^{3+} and Mn^{4+} species and the satellite [16,33,46], respectively. The accurate contents of surface Mn^{n+} and their molar ratios were calculated by a quantitative analysis method on the Mn $2p$ XPS spectra, as shown in Table 2. It is clearly observed that the preparation method had a great impact on the surface $\text{Mn}^{4+}/\text{Mn}^{3+}$ molar ratios of the products, with nanocasted Cu–Mn sample possessing the highest surface $\text{Mn}^{4+}/\text{Mn}^{3+}$ molar ratio (1.7) whereas the NaOH-derived sample showing the lowest value (0.9). Generally, manganese species in the form of $\text{Mn}^{4+}-\text{O}_{\text{ads}}$ Lewis acid–base pairs will be well dispersed on the catalyst surface [60] so that more adsorbed oxygen species will exist on the sample with higher $\text{Mn}^{4+}/\text{Mn}^{3+}$ molar ratio. The distribution of surface oxygen species can be obtained by investigating the result of O $1s$ XPS, as shown in Fig. 11c. For each sample, one can decompose the O $1s$ spectrum into three components at BE = 529.7, 531.0 and 532.3 eV, assignable to the surface lattice oxygen (O_{latt}), adsorbed oxygen (O_{ads}) and adsorbed OH groups or molecular water species, [16,41,45,60], respectively. The surface $\text{O}_{\text{ads}}/\text{O}_{\text{latt}}$ molar ratio (0.57) of the nanocasted Cu–Mn composite oxide was

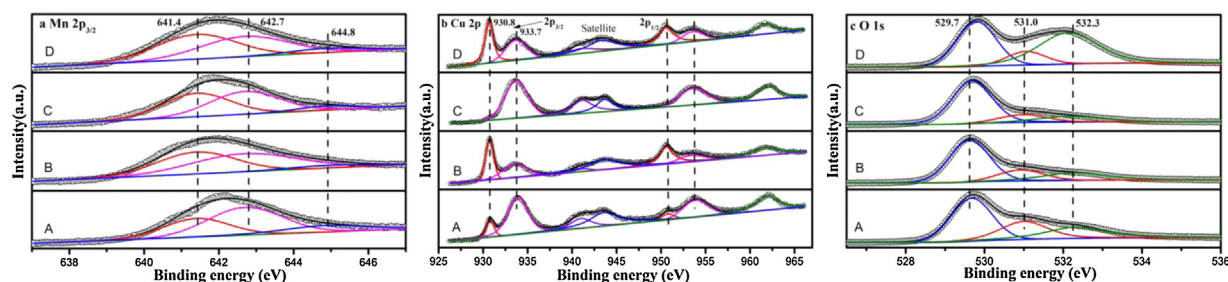


Fig. 11. (a) Mn $2p_{3/2}$, (b) Cu $2p$, (c) O $1s$ XPS spectra of (A) $\text{Cu}_{0.6}\text{Mn}$ -nanocasting, (B) $\text{Cu}_{0.6}\text{Mn}$ - Na_2CO_3 , (C) $\text{Cu}_{0.6}\text{Mn}$ -direct calcination, (D) $\text{Cu}_{0.6}\text{Mn}$ -NaOH.

much higher than that of other samples, indicating that the catalyst with a higher surface area maintained a more amount of electrophilic oxygen species which was beneficial for the enhancement in catalytic performance for deep oxidation reactions. Furthermore, the Cu 2p XPS spectra of as-prepared Cu–Mn oxides were illustrated in Fig. 10b. All spectra are characterized by two main region of Cu 2p_{1/2} (950–955 eV) and Cu 2p_{3/2} (930–935 eV), along with shake up satellite peaks centred at 940–945 and 960–964 eV. The Cu 2p_{3/2} band at 933.7 eV can be contributed to fully oxidized Cu²⁺ species which is also confirmed by the shake-up satellites at 944.5 eV, typical of Cu²⁺ species [61,62]. Another Cu 2p_{3/2} peak at 930.8 eV is clearly observed on the all samples except for direct-calcination-derived sample C and it can be ascribed to the generation of Cu⁺ species in the spinel structure (stabilized by Cu–Mn interactions) [62–64]. For sample C, well crystalized CuO was detected by XRD and TEM analysis and only a small part of spinel Cu–Mn oxide was existed which confirms the weak interaction of Cu–Mn in this catalyst so that no obvious peak about Cu⁺ is obtained. The electronic transfer between copper and manganese to provide a redox mechanism: Cu²⁺–Mn³⁺ ↔ Cu⁺–Mn⁴⁺ which is critical to catalytic reaction [64]. The oxidation of Mn³⁺/Mn⁴⁺ involves the adsorption of oxygen species, while that of Cu²⁺/Cu⁺ is associated with lattice oxygen. The formation of spinel structure is considered to provide this synergic effect which is also significantly promoted by the nanocasting method.

4. Conclusions

In conclusion, an advanced co-nanocasting method was applied to synthesize mesoporous Cu–Mn composite oxide with high surface area (121–266 m² g^{−1}). Compared with the referenced Cu–Mn oxides prepared by traditional methods with T₉₀ at 277–365 °C for deep oxidation of benzene and high E_a values (89.1–113.1 kJ mol^{−1}), the nanocasted catalyst exhibits the best activity with T₉₀ at 234 °C and the lowest E_a values (45.0 kJ mol^{−1}) which was attributed to its high surface area, rich porous structure, abundant oxygen adsorbed species, low temperature reducibility and strong interaction of Cu–Mn species promoted by nanocasting method. Moreover, the nanocasted catalyst showed better activity than the others when the water vapor was introduced in the feed gas. It is expected that the co-nanocasting method can be extended to the fabrication of other composite metal oxides catalyst with significantly enhanced catalytic activity.

Acknowledgements

This work was supported by the Strategic Project of Science and Technology of Chinese Academy of Sciences (no. XDB05050000), the 863 Hi-tech Research and Development Program of China (grant no. 2012AA062702; no. 2013AA031801) and the National Natural Science Foundation of China (NSFC) (no. 51272253; no. 51002154).

Appendix A. Supplementary data

Supplementary data associated with this article can be found, in the online version, at <http://dx.doi.org/10.1016/j.apcatb.2014.06.030>.

References

- [1] A.P. Altshuller, *Atmos. Environ.* (1967) 17 (1983) 2131–2165.
- [2] J. Kesselmeier, M. Staudt, *J. Atmos. Chem.* 33 (1999) 23–88.
- [3] J.E. Cometto-Muñiz, W.S. Cain, M.H. Abraham, *Indoor Air* 14 (2004) 108–117.
- [4] G. Leson, A.M. Winer, *J. Air Waste Manage. Assoc.* 41 (1991) 1045–1054.
- [5] K.L. Foster, R.G. Fuerman, J. Economy, S.M. Larson, M.J. Rood, *Chem. Mater.* 4 (1992) 1068–1073.
- [6] M.A. Hernández, J.A. Velasco, M. Asomoza, S. Solís, F. Rojas, V.H. Lara, *Ind. Eng. Chem. Res.* 43 (2004) 1779–1787.
- [7] K. Everaert, J. Baeyens, *J. Hazard. Mater.* 109 (2004) 113–139.
- [8] J.J. Spivey, *Ind. Eng. Chem. Res.* 26 (1987) 2165–2180.
- [9] S. Zuo, Q. Huang, R. Zhou, *Catal. Today* 139 (2008) 88–93.
- [10] H.S. Kim, T.W. Kim, H.L. Koh, S.H. Lee, B.R. Min, *Appl. Catal., A: Gen.* 280 (2005) 125–131.
- [11] B. Solsona, E. Aylon, R. Murillo, A.M. Mastral, A. Monzonis, S. Agouram, T.E. Davies, S.H. Taylor, T. Garcia, *J. Hazard. Mater.* 187 (2011) 544–552.
- [12] J.S. Yang, W.Y. Jung, G.D. Lee, S.S. Park, E.D. Jeong, H.G. Kim, S.-S. Hong, *J. Ind. Eng. Chem.* 14 (2008) 779–784.
- [13] T.-Y. Li, S.-J. Chiang, B.-J. Liaw, Y.-Z. Chen, *Appl. Catal., B: Environ.* 103 (2011) 143–148.
- [14] H.C. Genuino, S. Dharmarathna, E.C. Njagi, M.C. Mei, S.L. Suib, *J. Phys. Chem. C* 116 (2012) 12066–12078.
- [15] H. Li, G. Qi, X. Tana, X. Zhang, W. Huang, W. Li, Shen, *Appl. Catal., B: Environ.* 103 (2011) 54–61.
- [16] W. Xingyi, K. Qian, L. Dao, *Appl. Catal., B: Environ.* 86 (2009) 166–175.
- [17] Z. Wang, G. Shen, J. Li, H. Liu, Q. Wang, Y. Chen, *Appl. Catal., B: Environ.* 138–139 (2013) 253–259.
- [18] D. Delimaris, T. Ioannides, *Appl. Catal., B: Environ.* 84 (2008) 303–312.
- [19] L.F. Liotta, M. Ousmane, G. Di Carlo, G. Pantaleo, G. Deganello, G. Marci, L. Retaillieu, A. Giroir-Fendler, *Appl. Catal., A: Gen.* 347 (2008) 81–88.
- [20] L.F. Liotta, M. Ousmane, G. Di Carlo, G. Pantaleo, G. Deganello, A. Boreave, A. Giroir-Fendler, *Catal. Lett.* 127 (2008) 270–276.
- [21] Z. Zhao, X. Lin, R. Jin, G. Wang, T. Muhammad, *Appl. Catal., B: Environ.* 115–116 (2012) 53–62.
- [22] D.A. Aguilera, A. Perez, R. Molina, S. Moreno, *Appl. Catal., B: Environ.* 104 (2011) 144–150.
- [23] X. Yao, Y. Xiong, W. Zou, L. Zhang, S. Wu, X. Dong, F. Gao, Y. Deng, C. Tang, Z. Chen, L. Dong, Y. Chen, *Appl. Catal., B: Environ.* 144 (2014) 152–165.
- [24] A. Vasile, V. Bratan, C. Hornoiu, N.I. Ionescu, T. Yuzhakova, Á. Rédey, *Appl. Catal., B: Environ.* 140–141 (2013) 25–31.
- [25] A. Aranda, E. Aylon, B. Solsona, R. Murillo, A.M. Mastral, D.R. Sellick, S. Agouram, T. Garcia, S.H. Taylor, *Chem. Commun. (Camb.)* 48 (2012) 4704–4706.
- [26] M. Morales, B. Barbero, L. Cadus, *Appl. Catal., B: Environ.* 67 (2006) 229–236.
- [27] J.P. Holgado, F. Ternero, V.M. Gonzalez-de-laCruz, A. Caballero, *ACS Catal.* 3 (2013) 2169–2180.
- [28] Q. Zhang, I. Lee, J.B. Joo, F. Zaera, Y. Yin, *Acc. Chem. Res.* 46 (2012) 1816–1824.
- [29] D. Wang, P. Zhao, Y. Li, *Sci. Rep.* 1 (2011) 37.
- [30] X.-F. Yang, A. Wang, B. Qiao, J. Li, J. Liu, T. Zhang, *Acc. Chem. Res.* 46 (2013) 1740–1748.
- [31] R. Mu, Q. Fu, H. Xu, H. Zhang, Y. Huang, Z. Jiang, S. Zhang, D. Tan, X. Bao, *J. Am. Chem. Soc.* 133 (2011) 1978–1986.
- [32] Y. Liu, W. Cen, Z. Wu, X. Weng, H. Wang, *J. Phys. Chem. C* 116 (2012) 22930–22937.
- [33] Y. Zhang, Z. Qin, G. Wang, H. Zhu, M. Dong, S. Li, Z. Wu, Z. Li, Z. Wu, J. Zhang, T. Hu, W. Fan, J. Wang, *Appl. Catal., B: Environ.* 129 (2013) 172–181.
- [34] Y. Zhu, E. Kockrick, S. Kaskel, T. Ikoma, N. Hanagata, *J. Phys. Chem. C* 113 (2009) 5998–6002.
- [35] H. Yang, Y. Yan, F. Liu, R. Zhang, Y. Zhang, M. YanMeng, S. Li, B. Xie, D. Tu, Zhao, *J. Phys. Chem. B* 108 (2004) 17320–17328.
- [36] B. Puertolas, B. Solsona, S. Agouram, R. Murillo, A.M. Mastral, A. Aranda, S.H. Taylor, T. Garcia, *Appl. Catal., B: Environ.* 93 (2010) 395–405.
- [37] T. Garcia, S. Agouram, J.F. Sánchez-Royo, R. Murillo, A.M. Mastral, A. Aranda, I. Vázquez, A. Dejoz, B. Solsona, *Appl. Catal., A: Gen.* 386 (2010) 16–27.
- [38] S. Haffer, T. Waitz, M. Tiemann, *J. Phys. Chem. C* 114 (2010) 2075–2081.
- [39] E. Pellicer, E. Menéndez, J. Fornell, J. Nogués, A. Vantomme, K. Temst, J. Sort, *J. Phys. Chem. C* 117 (2013) 17084–17091.
- [40] S. Haffer, T. Walther, R. Köferstein, S. Ebbinghaus, M. Tiemann, *J. Phys. Chem. C* 117 (2013) 24471–24478.
- [41] W. Tang, X. Wu, D. Li, Z. Wang, G. Liu, H. Liu, Y. Chen, *J. Mater. Chem. A* 2 (2014) 2544–2554.
- [42] A. Fischereder, M.L. Martinez-Ricci, A. Wolosiuk, W. Haas, F. Hofer, G. Trimmel, G.J.A.A. Soler-Illia, *Chem. Mater.* 24 (2012) 1837–1845.
- [43] Z. Zhu, G. Lu, Z. Zhang, Y. Guo, Y. Guo, Y. Wang, *ACS Catal.* 3 (2013) 1154–1164.
- [44] Y. Liao, M. Fu, L. Chen, J. Wu, B. Huang, D. Ye, *Catal. Today* 216 (2013) 220–228.
- [45] Y. Liu, H. Dai, Y. Du, J. Deng, L. Zhang, Z. Zhao, C.T. Au, *J. Catal.* 287 (2012) 149–160.
- [46] Q. Ye, J. Zhao, F. Huo, D. Wang, S. Cheng, T. Kang, H. Dai, *Microporous Mesoporous Mater.* 172 (2013) 20–29.
- [47] F. Liu, S. Zuo, C. Wang, J. Li, F.-S. Xiao, C. Qi, *Appl. Catal., B: Environ.* 148–149 (2014) 106–113.
- [48] D.C. Golden, J.B. Dixon, C.C. Chen, *Clays Clay Miner.* 34 (1986) 511–520.
- [49] S. Ching, D.J. Petrovay, M.L. Jorgensen, S.L. Suib, *Inorg. Chem.* 36 (1997) 883–890.
- [50] D. Zhao, J. Feng, Q. Huo, N. Melosh, G.H. Fredrickson, B.F. Chmelka, G.D. Stucky, *Science* 279 (1998) 548–552.
- [51] T. Tsoncheva, L. Ivanova, J. Rosenholm, M. Linden, *Appl. Catal., B: Environ.* 89 (2009) 365–374.
- [52] W. Shen, X. Dong, Y. Zhu, H. Chen, J. Shi, *Microporous Mesoporous Mater.* 85 (2005) 157–162.
- [53] Y. Xia, H. Dai, L. Zhang, J. Deng, H. He, C.T. Au, *Appl. Catal., B: Environ.* 100 (2010) 229–237.
- [54] B. Bai, H. Arandian, J. Li, *Appl. Catal., B: Environ.* 142–143 (2013) 677–683.
- [55] W.-C. Li, A.-H. Lu, C. Weidenthaler, F. Schüth, *Chem. Mater.* 16 (2004) 5676–5681.

- [56] K. Ji, H. Dai, J. Deng, X. Li, Y. Wang, B. Gao, G. Bai, C.T. Au, *Appl. Catal., A: Gen.* 447–448 (2012) 41–48.
- [57] H. Tuysuz, M. Comotti, F. Schuth, *Chem. Commun.* 34 (2008) 4022–4024.
- [58] D. Delimaris, T. Ioannides, *Appl. Catal., B: Environ.* 89 (2009) 295–302.
- [59] A. Mirzaei, *Appl. Catal., A: Gen.* 253 (2003) 499–508.
- [60] Y. Liu, H. Dai, J. Deng, Y. Du, X. Li, Z. Zhao, Y. Wang, B. Gao, H. Yang, G. Guo, *Appl. Catal., B: Environ.* 140–141 (2013) 493–505.
- [61] M. Konsolakis, S.A. Carabineiro, P.B. Tavares, J.L. Figueiredo, *J. Hazard. Mater.* 261 (2013) 512–521.
- [62] H. Chen, X. Tong, Y. Li, *Appl. Catal., A: Gen.* 370 (2009) 59–65.
- [63] X. Qiu, M. Miyauchi, K. Sunada, M. Minoshima, M. Liu, Y. Lu, D. Li, Y. Shimodaira, Y. Hosogi, Y. Kuroda, K. Hashimoto, *ACS Nano* 6 (2011) 1609–1618.
- [64] S.A. Kondrat, T.E. Davies, Z. Zu, P. Boldrin, J.K. Bartley, A.F. Carley, S.H. Taylor, M.J. Rosseinsky, G.J. Hutchings, *J. Catal.* 281 (2011) 279–289.